ACS APPLIED MATERIALS & INTERFACES

Letter

www.acsami.org

# Preparation and Photocatalytic Activity of Robust Titania Monoliths for Water Remediation

Kazuya Nakata,*[,†,‡] Tomoya Kagawa,[†,§] Munetoshi Sakai,[†] Shanhu Liu,[‡] Tsuyoshi Ochiai,[†,‡] Hideki Sakai,[‡,§] Taketoshi Murakami,[†] Masahiko Abe,[‡,§] and Akira Fujishima[†,‡]

[†]Photocatalyst group, Kanagawa Academy of Science and Technology, KSP Building East 412, 3-2-1 Sakado, Takatsu-ku, Kawasaki, Kanagawa 213-0012, Japan

[‡]Research Institute for Science and Technology, Energy and Environment Photocatalyst Research Division, Tokyo University of Science, 1-3 Kagurazaka, Shinjuku-ku, Tokyo 162-8601, Japan

[§]Department of Pure and Applied Chemistry, Faculty of Science and Technology, Tokyo University of Science, Noda 278-8510, Japan

Supporting Information

**ABSTRACT:** $TiO_2$ monoliths were prepared, characterized, and evaluated for photocatalytic performance. The $TiO_2$ monoliths were found to have an interconnected void lattice and a bimodal porous structure with macropores and mesopores after calcination at 500−700 °C. Monoliths calcined at 500 °C had high specific surface area (93.1 $m^2$/g) and porosity (68%), which were maintained after calcination at 700−1100 °C (51−46%). The calcined monoliths had relatively high Vickers hardness (~104) despite their porous structure. Monoliths calcined at 500 and 700 °C exhibited high performance for methylene blue decolorization because of their high specific surface area.

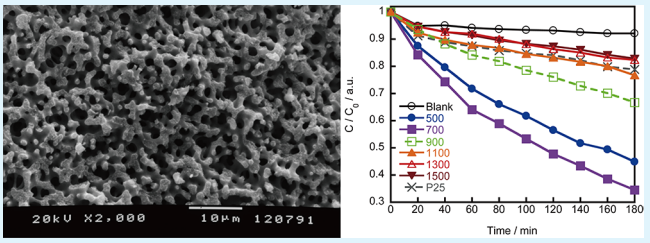


**KEYWORDS:** *titania, monolith, photocatalysis, water remediation*

A variety of chemical substances entering the water environment are giving cause for concern. Various contaminants such as dyes, detergents, pesticides, organochlorines, and aromatic hydrocarbons have been detected, and a number of these are suspected of being endocrine disrupting chemicals.[1−6] Among a number of water remediation methods, the photocatalytic oxidation of organic contaminants by titanium dioxide ($TiO_2$) has attracted much attention as a promising chemical procedure for environmental cleanup, and as an environmentally friendly method because it is able to decompose almost all organic contaminants with only photoenergy.[7−13] The oxidative decomposition of organic contaminants is mediated by holes photogenerated on the $TiO_2$ surface, which occur upon the absorption of UV light, and by a series of radical reactions initiated by active oxygen species such as hydroxyl radicals and superoxide ions.[14−25] Thus, $TiO_2$ photocatalysis is effective for the degradation of a wide range of organic contaminants in water. Furthermore, $TiO_2$ has chemical stability, long durability, nontoxicity, low cost, and transparency to visible light, which makes it preferential for practical applications.

Typically, oxidative decomposition of organic contaminants in water is performed by simple mixing of $TiO_2$ powder into the water.[26] This is an effective method because $TiO_2$ effectively contacts organic contaminants and absorbs light, leading to a high rate for the photocatalytic reaction. However, the small particle size of the powder means that a microfiltration step is necessary for catalyst recovery from the suspension after reaction, a difficult and laborious procedure. Moreover, inorganic powders frequently cause secondary pollution, which has hampered their practical application.

To preclude the problem of $TiO_2$ particle separation from wastewater, researchers have taken many approaches immobilize $TiO_2$ photocatalysts on various supporting matrices, such as ceramic foam, metal foam, zeolite, sand, glass media, and resins, among others.[27−31] However, typical preparation procedures require coating, soaking, precipitating, or spinning methods, which increases the preparation steps, and an intermediate layer between $TiO_2$ and the supporting matrix to bind them. Furthermore, the immobilized $TiO_2$ has less reactive surface area where it contacts with organic contaminants, leading to low photocatalytic performance. The immobilized $TiO_2$ may also be detached from the supporting matrix over long periods of operation, causing decreasing photocatalytic performance and secondary pollution.

To solve the above problems, self-supported porous $TiO_2$ framework monolithic materials are candidates for water remediation.[32] These have a high effective surface area because

**Received:** November 10, 2012
**Accepted:** January 9, 2013
**Published:** January 17, 2013

  

of their pores, which is an advantage for water remediation. Furthermore, the utilization of $TiO_2$ monoliths avoids the need to coat the $TiO_2$ particles onto supporting matrices, which suffer from the detachment of $TiO_2$ particles. In addition, with such monoliths the separation of $TiO_2$ particles from wastewater is also unnecessary. However, porous materials are typically fragile, which has hampered their practical use for long periods.

In this work, we have prepared self-supported robust $TiO_2$ monoliths with porous structures, and evaluated their photocatalytic performance using the decolorization of methylene blue.

$TiO_2$ monoliths were prepared as follows: titanium tetraisopropoxide (2.9 g, 10 mmol) was mixed with hydrochloric acid (529 $\mu$L, 6 mmol, 35 wt %), followed by stirring for 4 min in an ice-bath. Then, the solution was added to an aqueous solution (374 $\mu$L) containing polyethylene glycol (PEG, 93.4 mg, 9.34 $\mu$mol, average $M_w$ 10 000), and N-methyl formamide (NFA, 400 $\mu$L, 6.85 mmol) and stirred for a further 4 min. The solution was transferred to a Teflon-lined stainless steel vessel (25 mL), which was then heated at 60 °C for 24 h in an oven. The temperature then was increased to 200 °C and held for a further 24 h. After cooling, a white block was obtained and subsequently immersed in 1-propanol for 24 h to remove excess starting chemicals. The white block was dried in air for 1−3 weeks in a plastic box to avoid cracking caused by rapid drying, and then calcined at varying temperatures (500−1100 °C) for 5 h in air with a ramp rate of 1 °C/min. In the case of the samples calcined at 1300 and 1500 °C, the samples were first calcined at 1100 °C for 5 h with a ramp rate of 1 °C/min, cooled to room temperature, and then reheated to 1300 and 1500 °C, respectively, for 5 h with a ramp rate of 7 °C/min. For reference, P25 sample was prepared the press of P25 powder under high pressure in holder (cylinder shape, size: ø10 × 2.0 mm, adjusted by cutting) and then calcined at 700 °C for 16.7 h.

Photocatalytic performance was evaluated using the following procedure: $TiO_2$ monoliths (cylinder shape, size: ø10 × 2.0 mm, adjusted by cutting) were immersed in water containing methylene blue ($1 \times 10^{-5}$ M) for 120 h until it reached adsorption equilibrium. The methylene blue adsorbed $TiO_2$ monoliths were then dried and again soaked in water containing methylene blue ($1 \times 10^{-5}$ M) and illuminated with UV light (1 mW/cm$^2$). The concentration of methylene blue in the solution was monitored by the methylene blue absorption maximum at around 663 nm in its UV−vis absorption spectrum.

X-ray diffraction (XRD) patterns of the samples after calcination at different temperature are presented in Figure 1. The pattern of the sample calcined at 500 °C has peaks consistent with the anatase phase at $2\theta$ = 25.1, 37.8, 47.7, 53.8, and 55.2° that can be indexed to the (101), (004), (200), (105), and (211) crystal faces of anatase $TiO_2$, respectively. In contrast, samples calcined above 700 °C contained rutile phase $TiO_2$, exhibiting peaks at $2\theta$ = 27.5, 36.2, 39.3, 41.4, 44.1, 54.4, and 56.7° that can be indexed to the (110), (101), (200), (111), (210), (211), and (220) crystal faces of rutile $TiO_2$, respectively. The sharp peaks of the samples calcined above 700 °C indicated better crystallinity.

Figure 2 shows scanning electron microscope (SEM) images of the samples after calcination. An interconnected void lattice monolithic structure was observed after calcination at 500−1100 °C, as seen before calcination (see Figure 1S in the Supporting Information). During calcination at 1300 °C, the framework of the $TiO_2$ monolith became aggregated and the voids had shrunk, which caused the whole monolith structure to collapse. At the higher calcination temperature of 1500 °C, the voids had largely disappeared and formed large aggregated crystals. Note that typically, pores disappear at high temperatures such as 1100 °C, but the present porous structure still remained after calcination even at 1100 °C, which is advantageous to photocatalytic reaction (see below).

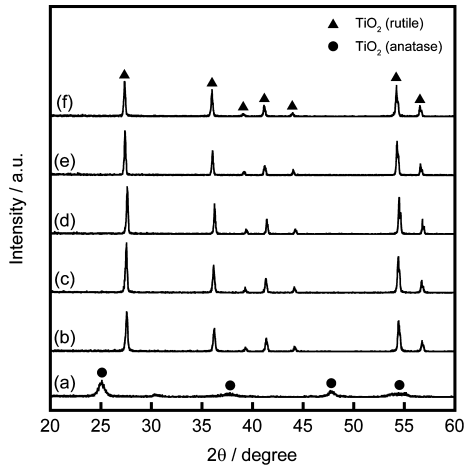


**Figure 1.** XRD patterns of samples calcined at (a) 500, (b) 700, (c) 900, (d) 1100, (e) 1300, and (f) 1500 °C.

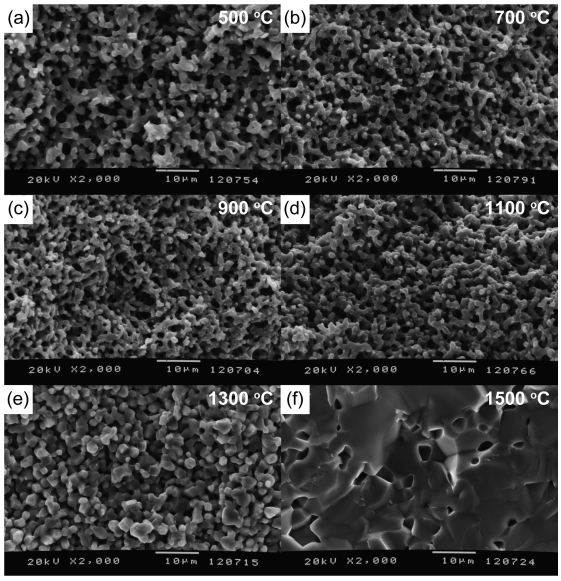


**Figure 2.** SEM images of samples calcined at (a) 500, (b) 700, (c) 900, (d) 1100, (e) 1300, and (f) 1500 °C.

The detailed structures of the frameworks of the $TiO_2$ monoliths were further examined by field-emission scanning electron microscopy (FE-SEM), as shown in Figure 3. After calcination at 500 °C, the $TiO_2$ monolith framework had a porous structure consisting of small particles with an average diameter of 23.1 nm. The average size of the particles increased to 119 nm after calcination at 700 °C, and framework had a porous structure with slightly larger pores than those of the sample calcined at 500 °C. After calcination at 900 and 1100 °C, the frameworks consisted of large crystals and were densely assembled and without pores. These changes of particle and


dx.doi.org/10.1021/am302654r | ACS Appl. Mater. Interfaces 2013, 5, 500−504

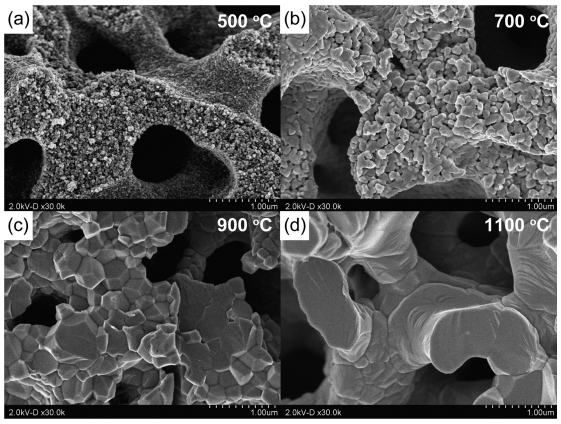


**Figure 3.** FE-SEM images of samples calcined at (a) 500, (b) 700, (c) 900, and (d) 1100 °C.

pore size were expected to affect porosity distribution and photocatalytic water purification activity (see below).

Figure 4 shows mercury intrusion porosimetry plots for the $TiO_2$ monoliths after calcination at 500−1500 °C. The $TiO_2$

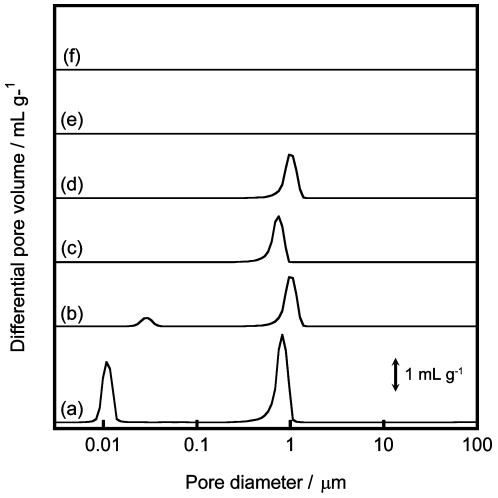


**Figure 4.** Mercury intrusion porosimetry plots (logarithmic scale on *x*-axis) of differential pore volume vs pore diameter for samples calcined at (a) 500, (b) 700, (c) 900, (d) 1100, (e) 1300, and (f) 1500 °C.

monoliths calcined at 500−1100 °C had macropores of around 1 $\mu$m in size, as observed in their SEM images. After calcination at 1300 and 1500 °C, the macropores disappeared because sintering collapsed the monolith structures, as confirmed by the SEM images. Furthermore, samples calcined at 500 and 700 °C had mesopores of around 10 and 30 nm in size, respectively. These originated from inside the framework of the $TiO_2$ monoliths, as observed in FE-SEM images (Figure 2). The mesopores disappeared at temperatures above 900 °C because of sintering, allowing the observed dense packing of $TiO_2$ crystals.

Figure 5a shows plots of specific surface areas and porosities for the samples after calcination at 500−1500 °C. The sample calcined at 500 °C had high specific surface area (93.1 $m^2/g$) and porosity (68%), attributed to the combination of mesopores inside the $TiO_2$ monolith framework and macropores in the monolith structure. The specific surface area was significantly decreased, to 6.47 $m^2/g$, after calcination at 700 °C due to sintering of the $TiO_2$ particles inside the monolith

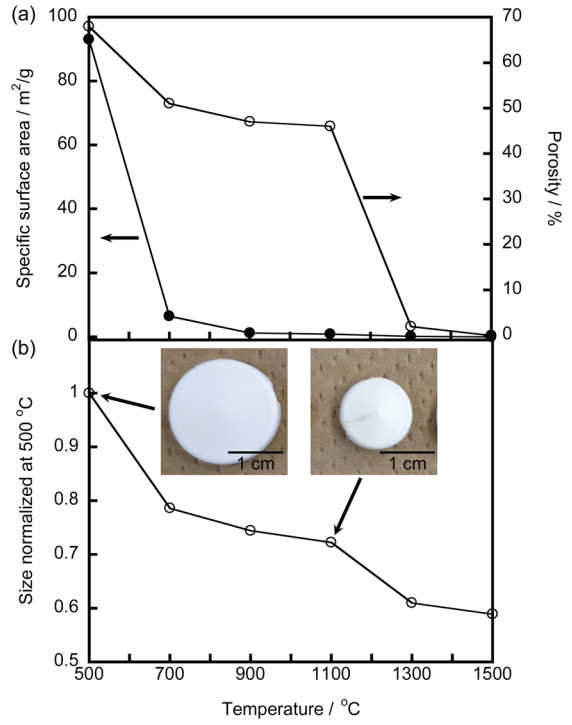


**Figure 5.** Plots of specific surface areas and porosities for samples calcined at 500−1500 °C.

framework. Further increase of calcination temperature decreased the specific surface area to below 0.01 $m^2/g$ after calcination at 1500 °C, as the voids greatly disappeared and large aggregated crystals formed. Porosity also decreased but maintained a high value (46−51%) after calcination at 700−1100 °C. However, it significantly decreased above 1300 °C because of the disappearance of macropores (<1% at 1500 °C).

Decrease in specific surface area and porosity caused shrinkage of the bulk size of the samples. Figure 5b shows plots of sample sizes. After calcination at 500 °C, the size of the sample decreased to 84% because of the removal of organic species, solvent evaporation, and crystallization. The size of the sample was significantly decreased after calcination at 700 °C, because of a decrease in the number of mesopores, as observed by FE-SEM and porosimetry measurements. After calcination above 900 °C, the volume of the sample continuously decreased due to sintering of the $TiO_2$ crystals. Above 1300 °C, the size of the sample was again significantly decreased by the disappearance of macropores.

The $TiO_2$ monoliths had high hardness after calcination. Figure 6 shows the Vickers hardness of the samples before and after calcination. Before calcination, the Vickers hardness of the monolith was only 2.6, and it slightly increased to 8.5 after calcination at 500 °C. However, further calcination significantly increased the Vickers hardness to 62.5, 99.2, and 104 after calcination at 700, 900, and 1100 °C, respectively. These high values were achieved by the crystallization of $TiO_2$, yet the samples nevertheless had a porous structure. Further calcination above 1300 °C drastically increased Vickers hardness because of the calcination of $TiO_2$ particles, although the monolith structure was collapsed.

Water purification testing was performed using samples calcined at 500−1500 °C to decolorize methylene blue as a model contaminant. Figure 7 shows the dependence of methylene blue concentration on the duration of UV light


dx.doi.org/10.1021/am302654r | ACS Appl. Mater. Interfaces 2013, 5, 500−504

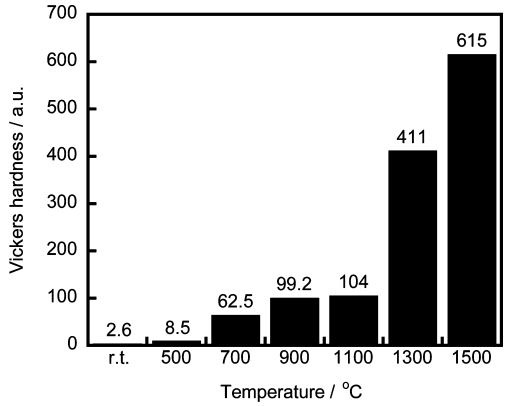


**Figure 6.** Vickers hardness for the samples before and after calcination at 500−1500 °C.

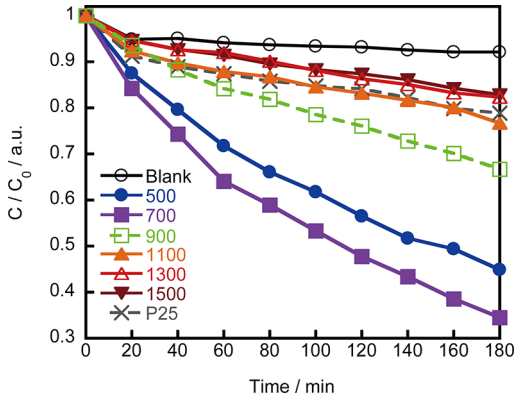


**Figure 7.** Decolorization of methylene blue as a model contaminant by samples calcined at 500−1500 °C and P25 sample.

illumination for the samples. A sample calcined at 500 °C had high performance for the decolorization of methylene blue, which was attributed to the high specific surface area originating from the combination of mesopores and macropores of the $TiO_2$ monolith. The sample calcined at 700 °C had superior decolorization to that of the sample calcined at 500 °C, which may have been due to the combination of better crystallinity and the continued presence of mesopores in the $TiO_2$ monolith. Typically, anatase phase $TiO_2$ shows better superior decolorization than rutile phase $TiO_2$. However, in this case, rutile $TiO_2$ of sample calcined at 700 °C had superior decolorization than sample calcined at 500 °C, even the sample calcined at 500 °C has anatase phase and higher specific surface area. Calcination at higher temperatures led to poorer photocatalytic decolorization performance due to disappearance of mesopores and macropores. Samples calcined at 900 and 1100 °C showed less decolorization compared to the samples calcined at 500 and 700 °C because the disappearance of the mesopores. Samples calcined at 1300 and 1500 °C showed further less decolorization because of the collapse not only the mesopores but also the monolith structure (macropores), even if the crystallinity of the samples is high. For reference, P25 sample which is prepared by press P25 powder was also evaluated for decolorization of methylene blue, which showed less decolorization than samples calcined at 500−1100 °C. This is because P25 sample has no meso and macropores, leading low specific surface area which is strongly related to photocatalytic activity. Note that reflectance for samples for 500−1500 °C (see Figure S2 in the Supporting Information) showed no significant difference at 365 nm. Thus, intrinsic optical absorption property for samples may not affect the photocatalytic decolorization. Penetration depth of UV irradiation is several millimeter as previously reported.[33] In our experimental, methylene blue adsorbed $TiO_2$ monolith was illuminated by UV light (365 nm, 1 mW/cm$^2$). We confirmed that penetration of UV light is 2 mm at least through $TiO_2$ monolith, which was checked by decolorization of methylene blue on front-back both sides of $TiO_2$ monolith, as shown in Figure S3 in the Supporting Information.

In conclusion, $TiO_2$ monoliths have been prepared, characterized, and evaluated for photocatalytic performance by methylene blue decolorization. SEM images showed that the samples had an interconnected void lattice monolith structure, before and after calcination in the range of 500−1100 °C. Mercury intrusion porosimetry revealed that the $TiO_2$ monoliths had a bimodal porous structure with macropores and mesopores, which was also supported by FE-SEM images. A $TiO_2$ monolith calcined at 500 °C had high specific surface area (93.1 m$^2$/g) and porosity (68%). Porosity was largely maintained after calcination at 700−1100 °C (46−51%). High Vickers hardness was observed for samples calcined at 700−1100 °C. $TiO_2$ monoliths calcined at 500 and 700 °C showed superior photocatalytic decolorization of methylene blue. The present $TiO_2$ monoliths realize both high hardness and high photocatalytic performance for water remediation.

## ■ ASSOCIATED CONTENT

### Supporting Information

SEM image of sample before calcination, feflectance spectra for samples calcined at 500−1500 °C, and photographs of methylene blue adsorbed sample calcined at 900 °C before UV light illumination for (a) front and (b) back side, and after UV light illumination for (c) front and (d) back side. These materials are available free of charge via the Internet at http://pubs.acs.org.

## ■ AUTHOR INFORMATION

### Corresponding Author

*Tel: +81-44-819-2020. Fax: +81-44-819-2038. E-mail: pg-nakata@newkast.or.jp.

### Notes

The authors declare no competing financial interest.

## ■ ACKNOWLEDGMENTS

This work was supported by a Grant-in-Aid for Scientific Research (B) from the Ministry of Education, Culture, Sports, Science and Technology of Japan, and Shanhu Liu acknowledges the Japan Society for the Promotion of Science (JSPS) for a Postdoctoral Fellowship for foreign Researchers. We thank Mr. Hidenori Saito for FE-SEM measurements.

## ■ REFERENCES

(1) Routledge, E. J.; Sumpter, J. P. *Environ. Toxicol. Chem.* **1996**, *15*, 241−248.
(2) Hong, C.-S.; Wang, Y.; Bush, B. *Chemosphere* **1998**, *36*, 1653−1667.
(3) Wang, Y.; Hong, C.-S. *Water Res.* **2000**, *34*, 2791−2797.
(4) Coleman, H. M.; Eggins, B. R.; Byrne, J. A.; Palmer, F. L.; King, E. *Appl. Catal. B: Environ.* **2000**, *24*, L1−L5.
(5) Yamamoto, T.; Yasuhara, A.; Shiraishi, H.; Nakasugi, O. *Chemosphere* **2001**, *42*, 415−418.

(6) Takai, Y.; Tsutsumi, O.; Ikezuki, Y.; Kamei, Y.; Osuga, Y.; Yano, T.; Taketan, Y. *Reprod. Toxicol.* **2000**, *15*, 71−74.
(7) Nakata, K.; Fujishima, A. *J. Photochem. Photobiol. C* **2012**, *13*, 169−189.
(8) Fujishima, A.; Zhang, X.; Tryk, D. A. *Surf. Sci. Rep.* **2008**, *63*, 515−582.
(9) Fujishima, A.; Zhang, X.; Tryk, D. A. *Int. J. Hydrogen Energy* **2007**, *32*, 2664−2672.
(10) Fujishima, A.; Zhang, X. *C. R. Chim.* **2006**, *9*, 750−760.
(11) Fujishima, A.; Rao, T. N.; Tryk, D. A. *Electrochim. Acta* **2000**, *45*, 4683−4690.
(12) Fujishima, A.; Rao, T. N.; Tryk, D. A. *J. Photochem. Photobiol. C* **2000**, *1*, 1−21−1−21.
(13) Nakata, K.; Ochiai, T.; Murakami, T.; Fujishima, A. *Electrochim. Acta* **2012**, *84*, 103−111.
(14) Zhao, T.; Liu, Z.; Nakata, K.; Nishimoto, S.; Murakami, T.; Zhao, Y.; Jiang, L.; Fujishima, A. *J. Mater. Chem.* **2010**, *20*, 5095−5099.
(15) Reddy, K. R.; Nakata, K.; Ochiai, T.; Murakami, T.; Tryk, D. A.; Fujishima, A. *J. Nanosci. Nanotechnol.* **2011**, *11*, 3692−3695.
(16) Reddy, K. R.; Nakata, K.; Ochiai, T.; Murakami, T.; Tryk, D. A.; Fujishima, A. *J. Nanosci. Nanotechnol.* **2010**, *10*, 7951−7957.
(17) Nakata, K.; Sakai, M.; Ochiai, T.; Murakami, T.; Takagi, K.; Fujishima, A. *Langmuir* **2011**, *27*, 3275−3278.
(18) Nakata, K.; Liu, B.; Ishikawa, Y.; Sakai, M.; Saito, H.; Ochiai, T.; Sakai, H.; Murakami, T.; Abe, M.; Takagi, K.; Fujishima, A. *Chem. Lett.* **2011**, *40*, 1107−1109.
(19) Nakata, K.; Liu, B.; Goto, Y.; Ochiai, T.; Sakai, M.; Sakai, H.; Murakami, T.; Abe, M.; Fujishima, A. *Chem. Lett.* **2011**, *40*, 1161−1162.
(20) Nakata, K.; Watanabe, N.; Yuda, Y.; Tryk, D. A.; Ochiai, T.; Murakami, T.; Koide, Y.; Fujishima, A. *J. Ceram. Soc. Jpn.* **2009**, *117*, 1203−1207.
(21) Nakata, K.; Nishimoto, S.; Yuda, Y.; Ochiai, T.; Murakami, T.; Fujishima, A. *Langmuir* **2010**, *26*, 11628−11630.
(22) Nakata, K.; Nishimoto, S.; Kubo, A.; Tryk, D. A.; Ochiai, T.; Murakami, T.; Fujishima, A. *Chem. Asian. J.* **2009**, *4*, 984−988.
(23) Liu, S.; Liu, B.; Nakata, K.; Ochiai, T.; Murakami, T.; Fujishima, A. *J. Nanomater.* **2012**, *2012*, 491927−1−5.
(24) Liu, B.; Nakata, K.; Sakai, M.; Saito, H.; Ochiai, T.; Murakami, T.; Takagi, K.; Fujishima, A. *Catal. Sci. Technol.* **2012**, *2*, 1933−1939.
(25) Liu, B.; Nakata, K.; Sakai, M.; Saito, H.; Ochiai, T.; Murakami, T.; Takagi, K.; Fujishima, A. *Langmuir* **2011**, *27*, 8500−8508.
(26) Li, X. Z.; Li, F. B. *Environ. Sci. Technol.* **2001**, *35*, 2381−2387.
(27) Fernández, A.; Lassaletta, G.; Jiménez, V. M.; Justo, A.; González-Elipe, A. R.; Herrmann, J. M.; Tahiri, H.; Ait-Ichou, Y. *Appl. Catal. B* **1995**, *7*, 49−63.
(28) Mozia, S.; Tomaszewska, M.; Morawski, A. W. *Dyes Pigm.* **2007**, *75*, 60−66.
(29) Behnajady, M. A.; Modirshahla, N.; Daneshvar, N.; Rabbani, M. *Chem. Eng. J.* **2007**, *127*, 167−176.
(30) Pozzo, R. L.; Baltanás, M. A.; Cassano, A. E. *Catal. Today* **1997**, *39*, 219−231.
(31) Anderson, M. A.; Gieselmann, M. J.; Xu, Q. *J. Membr. Sci.* **1988**, *39*, 243−258.
(32) Konishi, J.; Fujita, K.; Nakanishi, K.; Hirao, K.; Morisato, K.; Miyazaki, S.; Ohira, M. *J. Chromatogr. A* **2009**, *1216*, 7375−7383.
(33) Drisko, G. L.; Zelcer, A.; Wang, X.; Caruso, R. A.; Soler-Illia, G. J. d. A. A. *ACS Appl. Mater. Interfaces* **2012**, *4*, 4123−4130.